
Charge-Injection-Device Performance in the High-Energy-Neutron Environment of Laser-Fusion Experiments

Introduction

Electronic devices such as charge-coupled devices (CCDs)¹ or charge-injection devices (CIDs)² (the subject of this work) are used to image x rays emitted by laser-generated plasmas. The laser beam or beams interact with the target in various ways depending on the total energy- and intensity-generating, short-lived plasmas whose temperatures are such that either thermal or nonthermal x-ray emission takes place. X-ray imaging and x-ray spectroscopy are used in such research to diagnose conditions in the plasma. The laser–target interactions for laser intensities exceeding $\sim 10^{14}$ W/cm² result in plasma temperatures in the keV regime. During ablation and implosion of targets in laser-driven fusion experiments, stagnation core temperatures as high as ~ 10 keV can be obtained³ and are expected for conditions approaching ignition at the National Ignition Facility (NIF).⁴ Simultaneously with the x-ray emission, a burst of fusion-generated neutrons is emitted by the imploding target at the time of implosion stagnation. Maximum neutron yields of $\sim 10^{14}$ (DT, neutron energy 14.1 MeV) are currently generated at LLE’s Omega Laser Facility⁵ and are expected to be far exceeded on the NIF. At a yield of 10^{14} the neutron fluence at 1 m from the target, if unattenuated, is $\sim 8 \times 10^8$ neutrons/cm². In a typical $25\text{-}\mu\text{m} \times 25\text{-}\mu\text{m}$ pixel region of an imaging array, this neutron fluence corresponds to $\sim 5 \times 10^3$ neutrons per pixel. Clearly, if the solid-state device is sensitive to either the neutrons or neutron-induced γ rays or neutron-generated charged particles, this flux level could cause the device to be incapable of being used for imaging x rays.

The effects of ionizing radiation, both γ rays and charged particles, on silicon⁶ and on silicon-based photodetectors such as CCDs⁷ have been studied. γ rays and, therefore, neutron-induced γ rays, can cause bulk damage through Compton scattering of the γ rays by atomic electrons. The displaced Si atoms can permanently affect the noise level of the device or, if enough defects are created, render it unusable. While not immune to such effects, the unique architecture of the CID² makes it radiation tolerant.⁸ CID cameras able to withstand radiation levels of 10^6 -rad/h and 10^7 -rad accumulated dose are available.⁹

In this work the effects of high-energy (DT) neutrons on the CID cameras are examined. The experiments were performed on the 60-beam, UV OMEGA Laser.⁵ Implosions of DT-filled capsules on OMEGA can generate neutron yields of up to $\sim 10^{14}$ (Ref. 10). CID cameras are used on this system in a number of x-ray imaging diagnostics¹¹ at a range of distances (0.8 to 2.6 m) experiencing neutron fluences ranging from 10^7 to 10^9 neutrons/cm². It is demonstrated in this work that the resulting background and noise levels in the CID cameras are a function of the neutron fluence and that usable images are obtained throughout this fluence range. Furthermore, numerical processing of the images reduces neutron-induced noise in the x-ray images obtained during high-yield target experiments, extending the useful range to higher neutron yields/fluences.

Neutron-Induced Signal in CID Cameras

The CID cameras used in this work (model CID4150-DX3)¹² are the primary means of image acquisition at the Omega Laser Facility in a set of x-ray pinhole cameras (XPHCs)¹³ and an x-ray microscope that uses a Kirkpatrick–Baez reflection optic to obtain x-ray images. The x-ray microscope system, known as the gated monochromatic x-ray imager (GMXI),¹⁴ was used with CID cameras at the image plane in a time-integrating broadband mode. The sensitive x-ray range of the GMXI is ~ 2 to 7 keV, limited at the low end by transmission through a Be blast shield and at the high end by Ir-mirror reflectivity.¹⁴ The XPHCs are similarly limited at low x-ray energies but contain no high-energy mirror cutoff. Target-emission spectral shape makes the energy ranges comparable.

The model CID4150-DX3 is an 812×607 -pixel array of square photodiodes with $38.5\text{-}\mu\text{m}$ center-to-center spacing. The active area is $31.3 \times 23.2\text{ mm}^2$ and is housed inside an aluminum case with $48\text{-} \times 30\text{-mm}$ outside dimensions. The well depth for each pixel is $\sim 1.4 \times 10^6$ e–h pairs and the depletion region depth is $\sim 7\text{-}\mu\text{m}$ (Ref. 15). The sensors are front-side illuminated and have an equivalent dead layer of $\sim 1\text{-}\mu\text{m}$ Si (Ref. 15). The sensors do not have a phosphor coating, and all cameras in this study were operated in vacuum with a $25\text{-}\mu\text{m}$ -thick Be window in front of the sensor (toward target). In general the images in

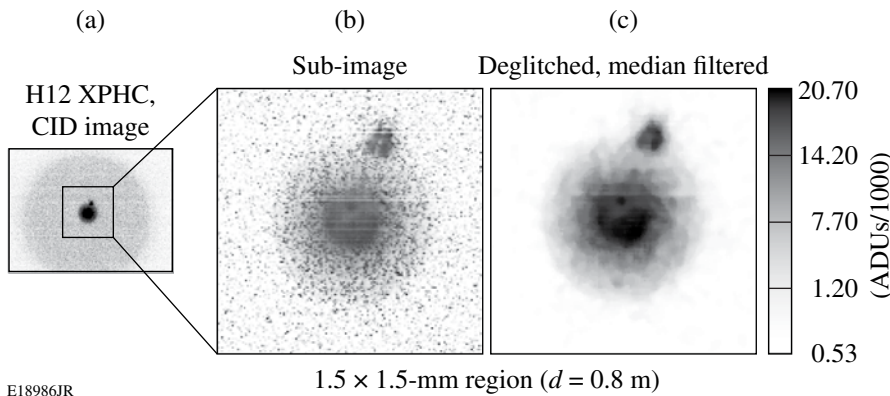
this study consist of an accumulated signal caused by x rays in the range of 2 to 7 keV.

Figures 123.57 and 123.58 show example x-ray images taken on typical D–T neutron-generating target experiments with an XPHC and the GMXI. The images are displayed in units of ADUs (analog-to-digital units). The XPHC image [Fig. 123.57(a)] is at a high neutron fluence ($\sim 4 \times 10^8$ neutrons/cm²) because of its proximity to the target (0.8 m), while the GMXI image [Fig. 123.58(a)] was taken at a much lower neutron fluence ($\sim 3 \times 10^7$ neutrons/cm²). Both target shots had the same approximate yield (3×10^{13} neutrons). The images are improved [Figs. 123.57(c) and 123.58(c)] by processing the images using deglitching and filtering (described later in the text).

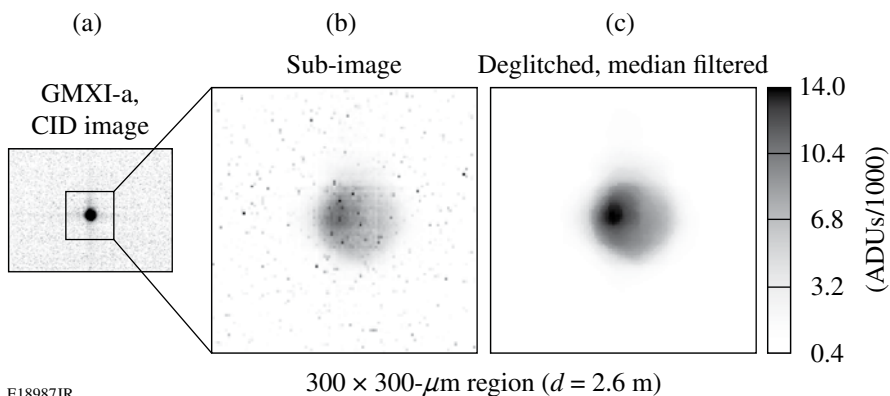
The neutron-induced effects in a set of images (~ 100) with neutron yields ranging from 3×10^{12} to 6×10^{13} , with CID cameras in both XPHCs and the GMXI, were determined as follows: The average signal level in the camera was determined in a 400×400 -pixel region not containing the x-ray image and

not shielded by any of the pinhole-camera support structure. The root-mean-square fluctuations (σ_{rms}) were computed from the variations of the mean signal in the same region. In all cases, the images are corrected for non-target-induced background (primarily dark current) by subtracting a frame taken before the laser shot (1.2 s before shot). The subtraction of the background frame is always a good idea and in the mode of operation of the CID cameras used in this work (uncooled) is essential. All values of background and σ_{rms} are plotted as a function of neutron fluence (yield over $4\pi d^2$, where d is the distance). Two CID cameras were in XPHC’s at a distance of 0.8 m to the target, and one was in an XPHC at a distance of 1.9 m. Additionally, two CID cameras were in the GMXI at a distance of 2.6 m. The DT-neutron yields were obtained from a fully cross-calibrated set of neutron detectors.¹⁶ The absolute neutron yields measured by these detectors are accurate to better than 10%.

Figure 123.59 shows the average neutron-induced signal level for all cameras as a function of neutron fluence. The signal level is seen to follow a straight line of slope ~ 1 , meaning



E18986JR



E18987JR

Figure 123.57

An x-ray image obtained with a CID camera in an OMEGA XPHC on a high-(DT) neutron-yield target shot (yield $\sim 3 \times 10^{13}$). (a) The full image with neutron-induced background and noise, (b) An unprocessed sub-image representing a 2×2 -mm region at the target. Single-pixel events are evident as are some line upsets. (c) A deglitched and median-filtered version of the same sub-image.

Figure 123.58

An x-ray image obtained with a CID camera in the GMXI on a target shot with similar yield to the XPHC image in Fig. 123.57 (yield $\sim 3 \times 10^{13}$). (a) Full image, (b) unprocessed sub-image representing a 500×500 - μm region at the target, and (c) a deglitched and median-filtered version of the same.

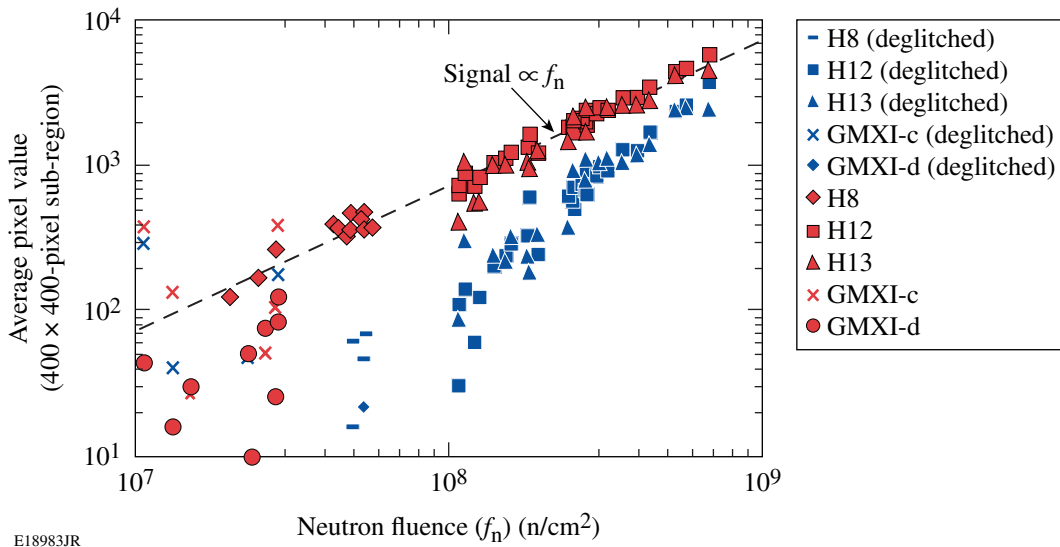


Figure 123.59

The average pixel value in ADUs for 400×400 -pixel regions in all of the CID cameras for regions not containing x-ray images as a function of the neutron fluence. The red (upper) values are from non-deglitched images and the blue (lower) values are from deglitched images.

it is proportional to the neutron fluence (f_n). As is noticed in Figs. 123.57 and 123.58, the neutron-induced signal consists of a near-single-pixel component as well as a more-uniform background. The single-pixel events are likely to be induced by n-p protons generated by neutron interaction with the $25\text{-}\mu\text{m}$ -thick Be window just in front of the CID sensor, while the uniform background is a consequence of n-gammas interacting with the CID sensor. (A study of the charged-particle sensitivity of this model of CID camera can be found in Fletcher *et al.*¹⁷). Jaanimagi *et al.*¹⁸ found a similar phenomenological effect on CCDs used for streak-camera recording at the Omega Facility.

The single-pixel events are effectively removed by deglitching the images. That is accomplished here by running a program that tests the values found in a 5×5 -pixel region. If the value of the pixel is greater than 1.25 times the median of that region, then the value is replaced by the median. This first step removes most of the high-signal-level single-pixel events. A second pass over the image, where the pixel value is replaced by the median of the pixel values resulting from the first pass, further reduces noise in the image. (More sophisticated noise-removal algorithms such as those compared in Chen and Yang¹⁹ are capable of even more thorough noise removal but are outside the scope of this article.) Examples of the improvements in the images are shown in Figs. 123.57(c) and 123.58(c). The lowering of the average signal level caused by deglitching is seen in the lower curve of values in Fig. 123.59 (deglitched values are those of step 1; no additional median filtering is applied).

The variation of the neutron-induced signal σ_{rms} is shown in Fig. 123.60. The variation is seen to follow a curve of slope $\sim 1/2$ making it proportional to $(f_n)^{1/2}$. Again, deglitching suppresses the noise by eliminating the high-signal-level single-pixel events (lower curve of values seen in Fig. 123.60). The maximum signal level detected in any given pixel (taken here to be $\sim 1.4 \times 10^6$ electron-hole pairs, corresponding to $\sim 20,000$ ADUs) limits the maximum detected x-ray signal. For instance, at 1 keV for an assumed e-h pair energy of 3.3 eV, the maximum number of absorbed photons is 4600. The maximum signal-to-noise ratio (SNR_{max}) achievable is therefore $\sim (n)^{1/2}$, where n is the number of photons absorbed. At 1 keV this is ~ 68 per pixel for the CID camera or, using the same argument, ~ 21 at 10 keV.

Figure 123.61 shows the computed SNR_{max} after background subtraction, with and without deglitching, for the same set of target experiments. Usable images are obtained for the highest neutron fluences encountered, with deglitching increasing the SNR by a factor of 3 or more. For comparison, the SNR_{max} achievable from photon-counting statistics for the 1-keV and 10-keV photon-energy cases are shown as horizontal dashed lines in Fig. 123.61. For the non-deglitched images the SNR is affected above neutron fluences of $\sim 3 \times 10^7$ neutrons/cm². For the deglitched images the SNR is restored to more than can be achieved with counting statistics alone for neutron fluences of up to $\sim 10^8$ neutrons/cm² for 1-keV photons or $\sim 3 \times 10^8$ neutrons/cm² for 10-keV photons.

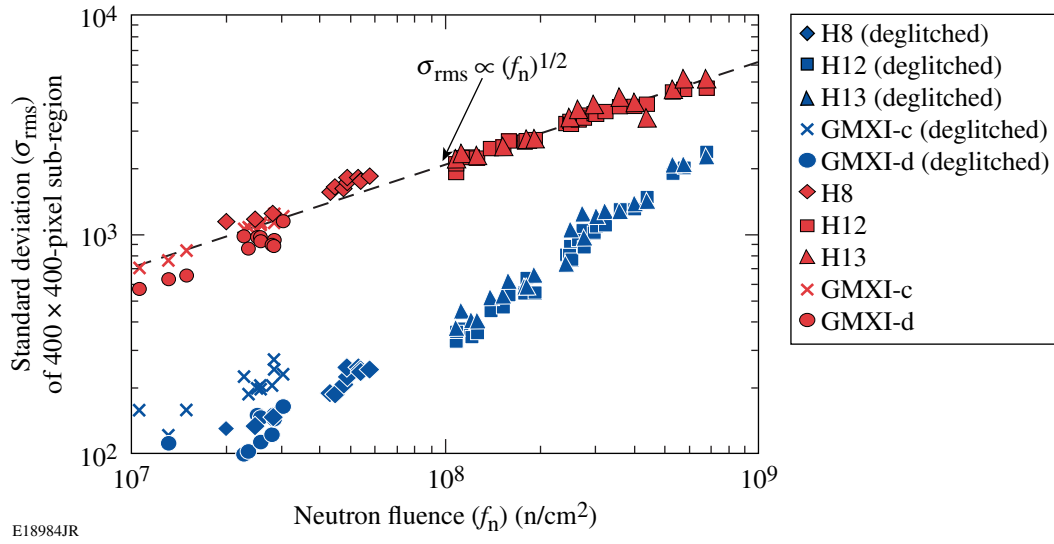


Figure 123.60
The standard deviation of the pixel values σ_{rms} as a function of neutron fluence for CID images from non-deglitched (red, upper) and deglitched (blue, lower) images.

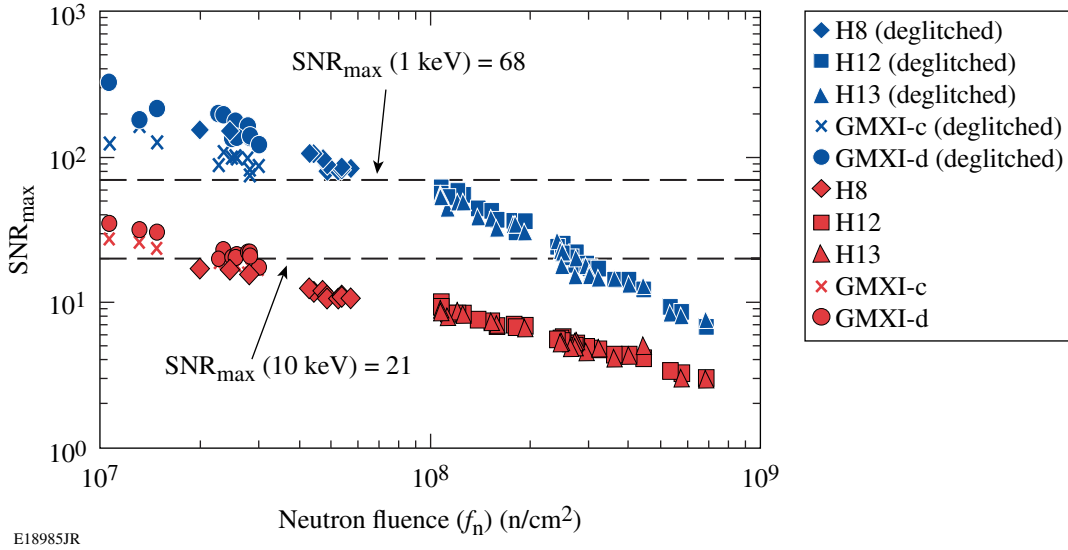
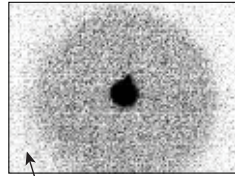


Figure 123.61
The computed maximum signal-to-noise ratio (SNR_{max}) as a function of neutron fluence from non-deglitched and deglitched images from all CID cameras. The dashed lines are the maximum SNR's obtainable from photon-counting statistics for 1- and 10-keV photons.

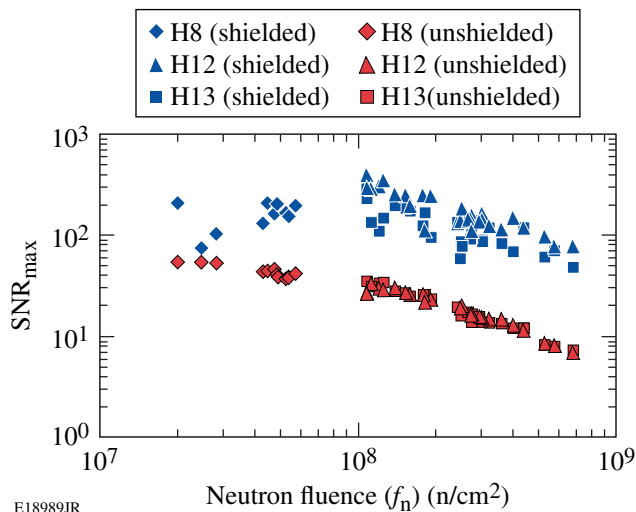
A further improvement of the SNR is achieved if the CID camera is shielded from the direct line of sight to the target with sufficient material to attenuate the neutron-induced signal. In the case described here (Fig. 123.62) the regions of the CID cameras in the XPHCs that are shielded by the body of the pinhole camera (~13 mm of stainless steel in the path) have a reduced background signal induced by the high-energy neutrons. For the cases shown, the shielding decreases the background and noise and increases the SNR, making it possible to use the CID cameras at inferred neutron fluences up to $\sim 10^{10}$ neutrons/cm² (extrapolation of the shielded SNR trend). At 1 m this corresponds to a neutron yield of $\sim 10^{15}$. To make practical use of shielding, however, the direct path to the target must be blocked. The diagnostic must therefore incorporate reflectors such as grazing-incidence mirrors, as in a KB microscope, or crystal-diffraction elements, as in a spectrometer.

undertaken at the Omega Laser Facility, where yields up to $\sim 10^{14}$ can be generated. The neutron-induced effects on the cameras are seen to scale with neutron fluence and therefore are inversely proportional to the square of the distance from the target to the camera. Deglitching the x-ray images obtained during high-energy neutron-target experiments reduces the noise and increases the fluence range that useful x-ray images can be obtained up to $\sim 3 \times 10^8$ neutrons/cm². Shielding the cameras from the direct line of sight to the target can further reduce the neutron-induced background, and an inferred yield of $\sim 10^{15}$ at 1 m could be tolerated if shielding comparable to or better than that used in this study is incorporated into the diagnostic. This, however, requires the use of reflectors or diffractors. This study indicates that the CID camera will be a useful means of obtaining time-integrated x-ray images on the NIF up to yields of $\sim 10^{15}$ or more depending on distance to the target and shielding.

H9 XPHC, CID image



Shielded region



E18989JR

Figure 123.62 The computed SNR_{max} for shielded and unshielded regions of CID cameras in OMEGA XPHCs as a function of neutron fluence. Both cases are for deglitched images.

Conclusions

The CID camera used in this work (model CID4150-DX3)¹¹ is seen to maintain usability in the high-energy neutron environment of DT-bearing target experiments currently being

ACKNOWLEDGMENT

This work was supported by the U.S. Department of Energy Office of Inertial Confinement Fusion under Cooperative Agreement No. DE-FC52-08NA28302, the University of Rochester, and the New York State Energy Research and Development Authority. The support of DOE does not constitute an endorsement by DOE of the views expressed in this article.

REFERENCES

1. J. R. Janesick *et al.*, *Opt. Eng.* **26**, 156 (1987).
2. J. Carbone *et al.*, in *Solid State Sensor Arrays: Development and Applications II*, edited by M. M. Blouke (SPIE, Bellingham, WA, 1998), Vol. 3301, pp. 90–99.
3. J. D. Lindl, *Inertial Confinement Fusion: The Quest for Ignition and Energy Gain Using Indirect Drive* (Springer-Verlag, New York, 1998).
4. W. J. Hogan, E. I. Moses, B. E. Warner, M. S. Sorem, and J. M. Soures, *Nucl. Fusion* **41**, 567 (2001).
5. T. R. Boehly, D. L. Brown, R. S. Craxton, R. L. Keck, J. P. Knauer, J. H. Kelly, T. J. Kessler, S. A. Kumpan, S. J. Loucks, S. A. Letzring, F. J. Marshall, R. L. McCrory, S. F. B. Morse, W. Seka, J. M. Soures, and C. P. Verdon, *Opt. Commun.* **133**, 495 (1997).
6. R. Korde *et al.*, *IEEE Trans. Nucl. Sci.* **36**, 2169 (1989).
7. J. Janesick, T. Elliott, and F. Pool, *IEEE Trans. Nucl. Sci.* **36**, 572 (1989).
8. J. Carbone, S. Czebiniaik, and R. Carta, in *Robotics and Remote Systems*, edited by L. M. Kostelnik, Proceedings of the Conference on Robotics and Remote Systems (American Nuclear Society, La Grange Park, IL, 1996), Vol. 43, pp. 43–50.
9. J. J. Zarnowski *et al.*, in *Charge-Coupled Devices and Solid State Optical Sensors IV*, edited by M. M. Blouke (SPIE, Bellingham, WA, 1994), Vol. 2172, pp. 187–198.

10. J. M. Soures, R. L. McCrory, C. P. Verdon, A. Babushkin, R. E. Bahr, T. R. Boehly, R. Boni, D. K. Bradley, D. L. Brown, R. S. Craxton, J. A. Delettrez, W. R. Donaldson, R. Epstein, P. A. Jaanimagi, S. D. Jacobs, K. Kearney, R. L. Keck, J. H. Kelly, T. J. Kessler, R. L. Kremens, J. P. Knauer, S. A. Kumpan, S. A. Letzring, D. J. Lonobile, S. J. Loucks, L. D. Lund, F. J. Marshall, P. W. McKenty, D. D. Meyerhofer, S. F. B. Morse, A. Okishev, S. Papernov, G. Pien, W. Seka, R. Short, M. J. Shoup III, M. Skeldon, S. Skupsky, A. W. Schmid, D. J. Smith, S. Swales, M. Wittman, and B. Yaakobi, *Phys. Plasmas* **3**, 2108 (1996).
11. F. J. Marshall, T. Ohki, D. McInnis, Z. Ninkov, and J. Carbone, *Rev. Sci. Instrum.* **72**, 713 (2001).
12. Thermo Fisher Scientific Instruments Division, CIDTEC Cameras and Imagers, Liverpool, NY 13088.
13. R. A. Forties and F. J. Marshall, *Rev. Sci. Instrum.* **76**, 073505 (2005).
14. F. J. Marshall and J. A. Oertel, *Rev. Sci. Instrum.* **68**, 735 (1997).
15. R. Forties, *2000 Summer Research Program for High School Juniors at the University of Rochester's Laboratory for Laser Energetics*, Rochester, NY, LLE Report No. 319, LLE Document No. DOE/SF/19460-383 (2000).
16. V. Yu. Glebov, C. Stoeckl, T. C. Sangster, S. Roberts, G. J. Schmid, R. A. Lerche, and M. J. Moran, *Rev. Sci. Instrum.* **75**, 3559 (2004).
17. K. A. Fletcher, B. Apker, S. Hammond, J. Punaro, F. J. Marshall, J. Laine, and R. Forties, *Rev. Sci. Instrum.* **78**, 063301 (2007).
18. P. A. Jaanimagi, R. Boni, and R. L. Keck, *Rev. Sci. Instrum.* **72**, 801 (2001).
19. S. Chen and X. Yang, *Opt. Eng.* **46**, 097003 (2007).